Opto-Electronic Science

CN 51-1800/O4 ISSN 2097-0382 (Print) ISSN 2097-4000 (Online)

Genetic algorithm assisted meta-atom design for high-performance metasurface optics

Zhenjie Yu, Moxin Li, Zhenyu Xing, Hao Gao, Zeyang Liu, Shiliang Pu, Hui Mao, Hong Cai, Qiang Ma, Wenqi Ren, Jiang Zhu and Cheng Zhang

Citation: Yu ZJ, Li MX, Xing ZY, et al. Genetic algorithm assisted meta-atom design for high-performance metasurface optics. *Opto-Electron Sci* **3**, 240016 (2024).

https://doi.org/10.29026/oes.2024.240016

Received: 17 April 2024; Accepted: 20 August 2024; Published online: 20 September 2024

Related articles

Opto-Electronic Science

Special Issue on Meta-lenses

Article

September 2024, Vol. 3, No. 9

DOI: 10.29026/oes.2024.240016

Genetic algorithm assisted meta-atom design for high-performance metasurface optics

Zhenjie Yu[1], Moxin Li[1], Zhenyu Xing[1], Hao Gao[1], Zeyang Liu[1], Shiliang Pu[2], Hui Mao[2], Hong Cai[2], Qiang Ma[2], Wenqi Ren[2], Jiang Zhu[2]* and Cheng Zhang[1]*

Metasurfaces, composed of planar arrays of intricately designed meta-atom structures, possess remarkable capabilities in controlling electromagnetic waves in various ways. A critical aspect of metasurface design involves selecting suitable meta-atoms to achieve target functionalities such as phase retardation, amplitude modulation, and polarization conversion. Conventional design processes often involve extensive parameter sweeping, a laborious and computationally intensive task heavily reliant on designer expertise and judgement. Here, we present an efficient genetic algorithm assisted meta-atom optimization method for high-performance metasurface optics, which is compatible to both single- and multi-objective device design tasks. We first employ the method for a single-objective design task and implement a high-efficiency Pancharatnam-Berry phase based metalens with an average focusing efficiency exceeding 80% in the visible spectrum. We then employ the method for a dual-objective metasurface design task and construct an efficient spin-multiplexed structural beam generator. The device is capable of generating zeroth-order and first-order Bessel beams respectively under right-handed and left-handed circular polarized illumination, with associated generation efficiencies surpassing 88%. Finally, we implement a wavelength and spin co-multiplexed four-channel metahologram capable of projecting two spin-multiplexed holographic images under each operational wavelength, with efficiencies over 50%. Our work offers a streamlined and easy-to-implement approach to meta-atom design and optimization, empowering designers to create diverse high-performance and multifunctional metasurface optics.

Keywords: metasurface; metalens; Bessel beam; metahologram; genetic algorithm

Yu ZJ, Li MX, Xing ZY et al. Genetic algorithm assisted meta-atom design for high-performance metasurface optics. *Opto-Electron Sci* **3**, 240016 (2024).

Introduction

Over the past decade, metasurfaces have garnered significant attention due to their capacity of manipulating various properties of electromagnetic (EM) waves[1–8], including phase, amplitude, and polarization. Such versatile manipulation is achieved through tailored light-matter interactions within their constituent sub-wavelength structures, commonly referred to as meta-atoms. By delicately designing and arranging these meta-atoms over a two-dimensional (2D) plane, metasurfaces can function as imaging lenses[9,10], hologram plates[11–13], structural beam generators[14–16], and more.

A crucial step in designing an optical metasurface is the identification of an individual meta-atom structure or a set of several meta-atom structures that can fulfill the device's target functionality[17]. Such operation is also

[1]School of Optical and Electronic Information & Wuhan National Laboratory for Optoelectronics, Huazhong University of Science and Technology, Wuhan 430074, China; [2]Hikvision Research Institute, Hangzhou 310051, China.

*Correspondence: J Zhu, Email: zhujiang.hri@hikvision.com; C Zhang, Email: cheng.zhang@hust.edu.cn

Received: 17 April 2024; Accepted: 20 August 2024; Published online: 20 September 2024

known as the establishment of meta-atom library. However, the process of establishing a meta-atom library is often cumbersome and heavily reliant on the designer's experience. Take the task of designing a nanofin-shaped meta-atom library as an example. The process typically begins with selecting appropriate constituent materials for both the meta-atom and its substrate. Subsequently, it involves simulating and analyzing the EM responses of various meta-atoms with different combinations of geometric parameters such as height, period, and cross-sectional dimensions (lateral width and length in the case of a nanofin structure). For instance, if we assume sampling of 50 points for each geometric parameter of the nanofin, it would necessitate a total of 6250000 sweeping loops to complete the EM simulation process. Furthermore, the computational workload would escalate with the substitution of materials, leading to an even greater number of calculations. Following the collection of EM responses from various meta-atoms, the designer needs to analyze the data to identify meta-atom structures that can best support the intended functionality of the metasurface. This typically involves selecting meta-atoms with high transmission efficiencies, specific phase-shift modulation values, targeted polarization conversion functionalities, and so on. In practice, conducting a comprehensive parameter sweeping is often impractical. Designers typically opt to explore only a portion of the meta-atom parameter space based on existing literature or their previous design experiences. However, this approach heavily relies on the designer's skill and expertise, and may result in sub-optimal solutions, particularly for complex design tasks targeting at the modulation of multiple state parameters of an EM wave and involving the selection of a group of different meta-atom structures. Consequently, there is a pressing need for more efficient and systematic approaches to meta-atom library design to streamline the structure searching process and enhance the performance of metasurface optics.

To mitigate the afore-mentioned limitations, various inverse design methods have been employed to facilitate meta-atom library establishment[18,19]. Inverse design approaches can be roughly classified into two categories: machine learning-based methods[18] and optimization-based methods[19]. In machine learning-based inverse designs, trained models can be utilized to predict the responses of different meta-atoms[20,21] or directly generate the structure parameters of required meta-atoms[22,23]. This method offers significantly faster computational speed compared to conventional EM simulations, but requires substantial time and computational resources to collect datasets and construct the model. Additionally, the trained model is typically only applicable to pre-determined meta-atom structures and constituent materials[24]. Optimization-based algorithms are another common approach for inverse design of meta-atoms and can be broadly categorized into gradient-based ones and gradient-free ones. Gradient-based optimization algorithms, such as topology optimization, have been widely applied in designing freeform meta-atom structures[25–27]. However, these methods are susceptible to getting trapped in local optima and may perform poorly in multi-objective design tasks[28]. In contrast, gradient-free optimization algorithms such as genetic algorithm[29], ant colony optimization[30], particle swarm optimization[31], possess global search capability and are more suitable for addressing multi-objective optimization problems.

Here, we propose a genetic algorithm assisted meta-atom inverse design method that is suitable for both single-objective and multi-objective metasurface design tasks. Genetic algorithm (GA), as a type of gradient-free optimization algorithm, mimics the process of biological evolution and natural selection[32,33]. By its exceptional global search capability, multi-core parallel processing ability, and compatibility with multi-objective optimization, GA has been applied to inverse design meta-atoms with regular[34] and binary[35,36] patterns, as well as freeform structures[28]. In this work, we incorporate all the structural parameters (e.g., material, period, height, cross-sectional dimensions, etc.) of meta-atoms as optimization variables, aiming to identify globally optimized structures of regular-shaped meta-atoms rather than increasing the shape complexity. We first perform a single-objective optimization task and inverse design a meta-atom structure that maintains high polarization conversion efficiency over a wide wavelength range (85% on average from 450 nm to 650 nm). Using the obtained meta-atom, we construct a Pancharatnam-Berry (PB) phase-based metalens showing diffraction-limited focusing capability and offering an averaged focusing efficiency of 80.76% in the visible spectrum. Then, we conduct a multi-objective optimization task and establish a meta-atom library consisting of 8 different nano-structures. These structures are selected to exhibit high transmission efficiency while imparting phase shift modulation evenly distributed over 0 to 2π on a free-space incident light at 532 nm. Utilizing the obtained meta-atom library, we implement a

spin-multiplexed dual-beam generator capable of producing zeroth-order and first-order Bessel beams under right-handed circularly polarized (RCP) and left-handed circularly polarized (LCP) illumination, respectively. The profiles of the generated Bessel beams align well with theoretical predictions, and the efficiencies of the two generation channels reach 88.07% and 90.72%, respectively. Finally, we undertake a more complex task of designing a wavelength and spin co-multiplexed four-channel metahologram that operates at free-space wavelengths of 532 nm and 633 nm. The device can project four independent holographic images based on the combination of free-space wavelength and spin state of the illumination light, exhibiting operational efficiencies exceeding 50% under green illumination and 60% under red illumination. Our work provides an effective and easy-to-implement approach for an array of meta-atom design and optimization tasks, facilitating designers in creating high-performance and multifunctional metasurface optics.

Results and discussion

Flowchart of the GA-based meta-atom inverse design process

The flowchart of the GA-based meta-atom design algorithm is illustrated in Fig. 1. The algorithm begins with the random initialization of a population consisting of a certain number of different individuals (IND_1, IND_2, ..., IND_n). The population size (i.e., the number of individuals contained in the population) determines how many electromagnetic (EM) simulations the algorithm will perform during each iteration. Population size affects the search capability of the GA algorithm. Expanding the population size enhances the search capability but reduces the algorithm's convergence speed. In practice, designers need to choose a proper population size to strike a balance between the search capability and convergence speed of the algorithm. In this study, we choose a population size of 50 for the first two tasks, and 100 for the 3rd task. In the task of identifying a single meta-atom structure, each individual contains a set of parameters describing the single meta-atom, including its constituent material, period, height, cross-sectional dimensions, etc. In the task of identifying a group of meta-atom structures, each individual contains a full set of parameters describing all the meta-atoms. Considering practical device implementation, structures within the same meta-atom library will be set to have the same constituent material, height, and period. For instance, in the identification of a group of rectangular-shaped nanofins, each individual will contain variables that are material (m), period (p), height (h), and various combinations of lateral length (l) and width (w) of the rectangular-shaped nanofins. The number of combinations is determined by the number of structures in the meta-atom library under construction.

After a population is initialized, the EM response of each individual within the population will be calculated through numerical simulation. Various simulation methods, including rigorous coupled wave analysis (RCWA), finite element method (FEM), and finite-difference time-domain method (FDTD), can be employed for this purpose. In this study, we opt to use RCWA. To evaluate the EM response and performance of each individual, fitness functions are designed according to the target functionalities of the metasurface under study. In single-objective design tasks, individuals which exhibit smaller fitness function values are considered as high-performance ones. In multi-objective design tasks, distinct fitness functions are respectively designed for different design objectives. The performance of an individual is evaluated by considering the values of all associated fitness functions. In this study, we employ non-dominated sorting[37] for the above purpose. As schematically illustrated in Fig. 1, both the blue and yellow dots represent the individuals evaluated in each iteration for a dual-objective design task, and the coordinate of each point is determined by the values of the two fitness functions respectively corresponding to each design objective. In contrast to the yellow dots, the blue dots represent non-dominated front. A key feature of such front is that its constituent points cannot exhibit reduced value along one axis (i.e., improved performance in one objective) without increasing the values along the other axes (i.e., scarified performance in the other objectives). The blue dots are labeled as rank 1. When ignoring the blue dots, the yellow dots can form a new non-dominated front and they are labeled as rank 2. All individuals in one population can be ranked using such manner. Individuals corresponding to higher ranking (smaller rank number) are considered as better performance. For individuals of the same ranking, their performance is further evaluated by their crowding distances (a measure of how close an individual is to its neighbors). The one with a larger crowding distance is considered better. We choose

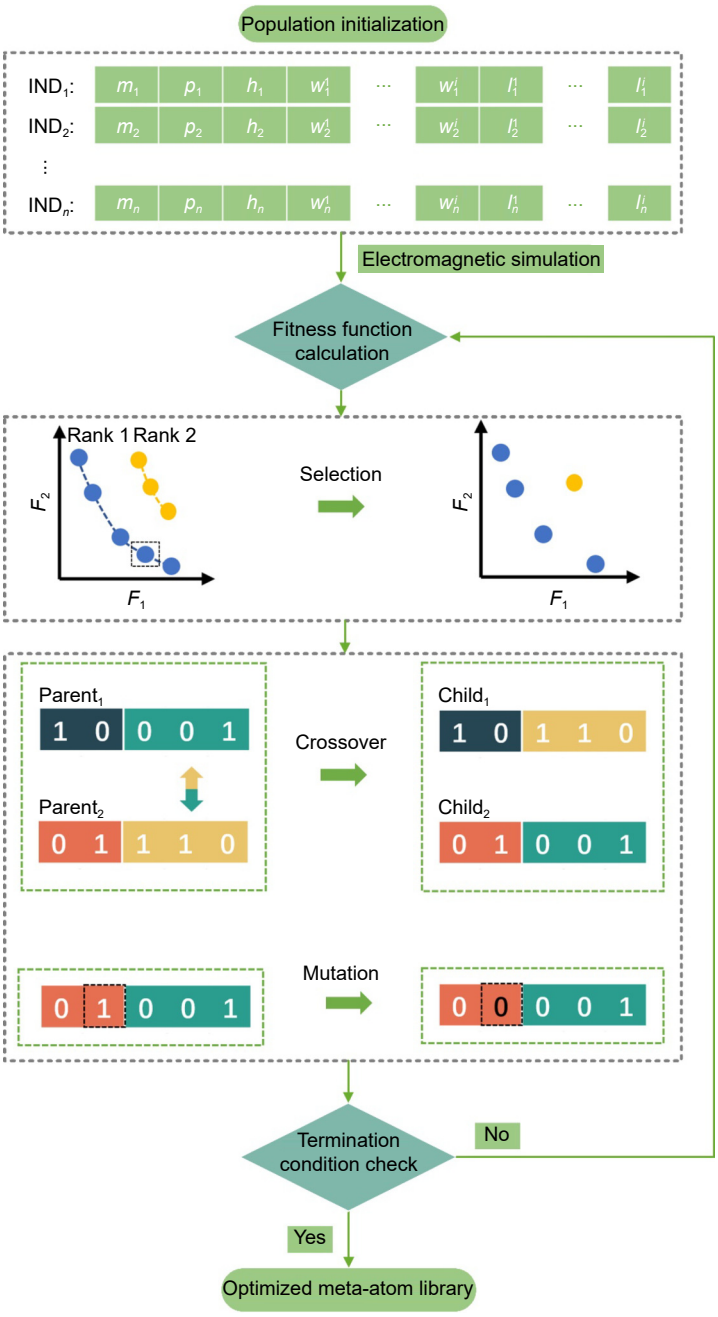

Fig. 1 | Flowchart illustrating the genetic algorithm-based meta-atom design process. The algorithm commences with the random initialization of a population, where each individual is defined by parameters such as material (m), period (p), height (h), and lateral sizes (w_1, w_2, …, w_n, l_1, l_2, ..., l_n) that characterize meta-atom structures. Electromagnetic responses are simulated for each individual, and their performance is assessed via associated fitness functions. In single-objective tasks, lower fitness function values denote superior performance, while in multi-objective tasks, non-dominated sorting is employed. Blue and yellow dots represent individuals evaluated in iterations for a dual-objective task, with their coordinates representing the associated fitness function values. The blue dots constitute the non-dominated front (rank 1), wherein improving one objective necessitates compromising others. Ignoring the blue dots yields a new non-dominated front (rank 2) represented by the yellow dots. Such ranking aids in assessing individual performance considering all associated fitness functions, with crowding distances further differentiating performance within the same ranking. For instance, the blue point within the dashed box exhibits a lower crowding distance, indicating poorer performance compared to other blue dots of the same rank. Tournament selection identifies parents for generating the next generation through crossover and mutation. During crossover, two parents exchange parts of their chromosomes to produce two children, while in the mutation step, genes in each child's chromosome are randomly altered. For simplicity, the chromosome is represented using binary notation. Iterations persist until termination conditions are met, resulting in an optimized meta-atom library.

tournament selection[38] to select parents to generate the next generation, where two individuals are randomly chosen from the population and the higher-performance one is selected as the parent. Such comparison process is repeated same number as the population size to select a group of parents.

In the next step, the selected parents will produce the next generation through crossover and mutation. In this study, we choose the classic combination of simulated binary crossover[39] and polynomial mutation[40]. For ease of description, the set of parameters in each parent individual can be referred to as a chromosome and each parameter can be referred to as a gene. In the crossover operation, two parents exchange parts of their chromosomes to generate two children. In the subsequent mutation step, the gene in the chromosome of each child is randomly changed.

When the overall performance of a population almost no longer improves with iteration, we determine that the algorithm converges and the optimization process will terminate. For a single-objective design task, the value of the defined fitness function is the standard for measuring the performance of a population. For a multi-objective design task, hypervolume is often used to evaluate the performance of a population[41]. It is defined as the volume of the hypercube enclosed by all points in the non-dominated front and a reference point in the design objective space. A higher hypervolume value indicates better performance of a population.

High-efficiency broadband PB phase metalens in the visible

We will first employ the developed GA-assisted meta-atom design method to construct a high-efficiency and broadband metalens over the visible region (450 nm to 650 nm), which operates based on the Pancharatnam–Berry (PB) phase modulation mechanism[42]. One core step in designing such a PB-phase-based metalens that can efficiently operate from 450 nm to 650 nm is to identify a meta-atom structure of high polarization conversion efficiency (PCE) over the above target wavelength range. PCE is an important metric[43] for evaluating the performance of meta-atoms that provide polarization-dependent EM responses, and can be defined as:

$$PCE(\lambda) = \frac{I_{\mathrm{P}}(\lambda)}{I_{\mathrm{Total}}(\lambda)} T(\lambda) \ , \tag{1}$$

here, I_{Total} and I_{P} represent the total intensity of the transmitted light through the meta-atom and the intensity of a specific polarization component in the transmitted light, respectively. T is the transmittance of the meta-atom.

In this design task, we choose to use nanofin-shaped meta-atom structure with a rectangular cross-section (Fig. 2(a)), by its ability to provide anisotropic (polarization-dependent) EM response. In a conventional meta-atom library design process requiring iterative parameter sweeping through EM simulation, the meta-atom's PCE is typically evaluated at a single wavelength (e.g., central wavelength of the target operational band) to reduce the computational workload. Afterwards, the selected meta-atom structure is then evaluated again for its broadband performance. However, in some cases, structures that exhibit high PCEs at a single wavelength may not perform well over a broadband. In this work, we will leverage the developed GA-assisted approach and directly take into account the meta-atom's overall performance in the target operational band by constructing a fitness function (F) that evaluates the meta-atom's averaged PCE value over the visible ($\mathrm{PCE_{vis}}$).

$$F = 1 - PCE_{\mathrm{vis}} \ , \tag{2}$$

when calculating the $\mathrm{PCE_{vis}}$, 11 sampling points are selected with an equal wavelength interval (20 nm) within the target band (450 nm to 650 nm). The variables of the GA algorithm include the constituent material (m), period (p), height (h), as well as the lateral length (l) and width (w) of the nanofin-shaped meta-atom. We select seven commonly-used transparent dielectrics in the visible as the candidate constituent materials[44–50], which are MgF_2, TiO_2, Ta_2O_5, HfO_2, ZnO, Al_2O_3, and Si_3N_4. As a variable of the individual, each material is assigned a number from 0 to 6. When calculating the EM response of a certain individual, the associated dielectric constant of the specific material with the designated number is used. The ranges of variation for p and h are respectively set to be 200–449 nm and 100–1000 nm. The ranges of variation for the cross-sectional dimensional (w and l) are all constrained within 50 ~ (p − 40) nm. Figure 2(b) depicts the convergence process of the optimization process, where algorithm convergence is achieved after approximately 75 iterations. For the clarity of display, we plot four curves as a function of iteration number, namely, the polarization conversion efficiency ($\mathrm{PCE_{opt}}$) and fitness function value (F_{opt}) of the optimal individual in each iteration, and the averaged polarization conversion

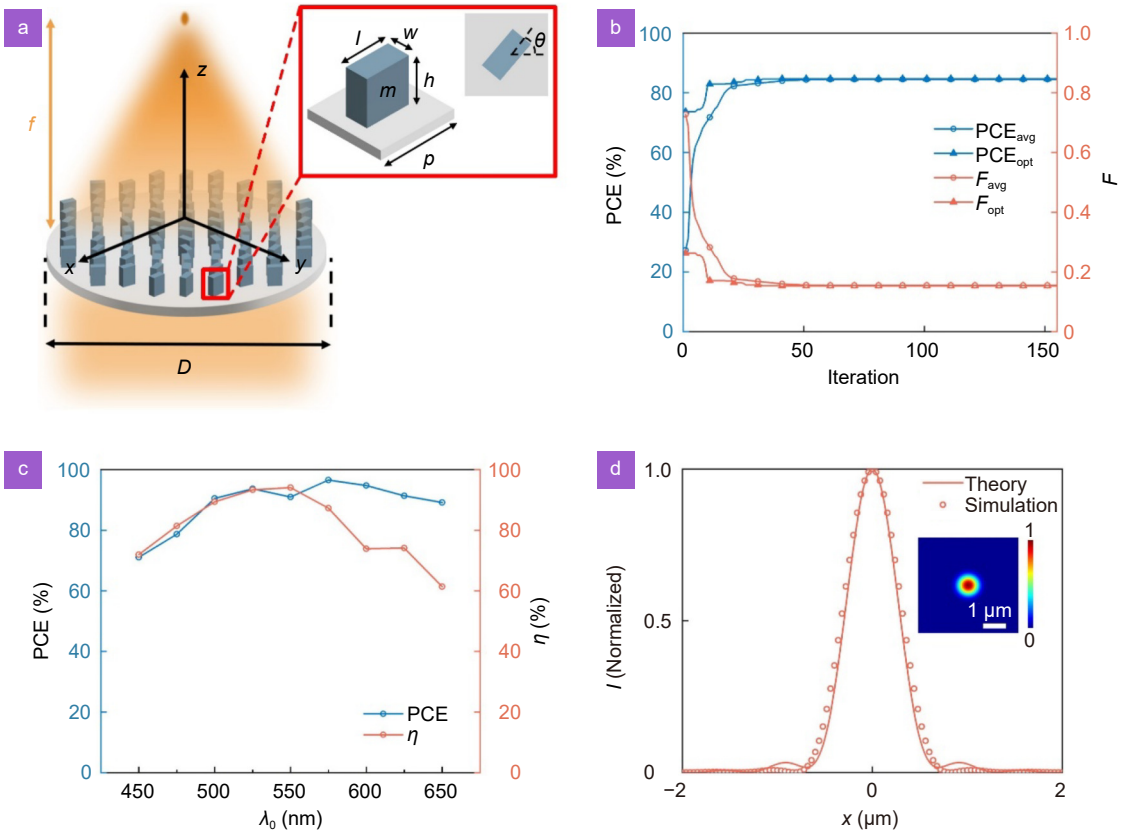

Fig. 2 | High-efficiency broadband PB phase metalens in the visible. (**a**) Schematic representation of the focusing metalens with a diameter D and focal length f. Inset: Schematic representation of a nanofin-shaped meta-atom structure with a constituent material m, period p, height h, as well as cross-sectional length l and width w. The meta-atom is set to have an in-plane rotation angle of θ, and will impart a phase modulation of 2θ over a circularly-polarized incident light based on the Pancharatnam–Berry (PB) phase modulation mechanism. (**b**) Convergence plot of the optimization process. Four different evaluation metrics, which are the polarization conversion efficiency (PCE_{opt}) and fitness function value (F_{opt}) of the optimal individual in each iteration, and the averaged polarization conversion efficiency (PCE_{avg}) and averaged fitness function value (F_{avg}) over the whole population in each iteration, all get flatten after approximately 75 iterations. (**c**) PCE of the inverse designed meta-atom (blue curve) and simulated focusing efficiency (η) of the metalens (orange curve) as a function of free-space illumination wavelength. (**d**) Intensity distribution at the focal plane along the x-axis (orange dots) for the constructed PB phase metalens, simulated at free-space illumination of λ_0 = 532 nm. Theoretical prediction (orange solid line) is shown for comparison. Inset: 2D intensity distribution at the focal plane.

efficiency (PCE_{avg}) and averaged fitness function value (F_{avg}) over the whole population in each iteration. The finally designed meta-atom structure employs TiO_2 as its constituent material, and has a height of h = 1000 nm, period of p = 241 nm, lateral dimension (w, l) = (111 nm, 201 nm). As displayed in Fig. 2(c) (blue curve), PCE of the designed meta-atom structure in the target band (450 nm to 650 nm) is maintained higher than 70%, with an averaged value of 85.12%.

Next, we will use the designed meta-atom to construct a PB-phase-based metalens. The required phase profile modulation of a metalens, ϕ_{lens}, can be expressed as:

$$\phi_{lens}(x,y) = -\frac{2\pi}{\lambda_0}\left(\sqrt{x^2+y^2+f^2}-f\right), \qquad (3)$$

where, x and y are in-plane distances along orthogonal directions from the center of the lens, given incident light propagating along the positive z-direction. Here, the designed metalens occupies a circular area with a diameter of D = 100 μm, and has a focal length of f = 100 μm at free-space wavelength of λ_0 = 532 nm. To implement the required phase modulation profile, the in-plane rotation angle of each nano-fin structure is set to be half of the required phase shift value at the center of the structure based on the PB phase modulation mechanism.

The performance of the constructed metalens is evaluated through FDTD simulation, where a RCP light is incident onto the metalens along positive z-axis. For all constructed metasurfaces in this study, the substrate material is fused silica (SiO_2), chosen for its excellent optical transparency within the wavelength range of study in

this work. During the FDTD simulation, the incident light source is placed inside the fused silica substrate. The intensity distribution at the metalens' focal plane reveals a circularly-symmetric focal spot (Fig. 2(d)), characterized by a cross section that closely matches the intensity distribution theoretically predicted for a diffraction-limited lens with the same numerical aperture (*NA*). We further evaluate the device's focusing efficiency over the target band. The focusing efficiency, η, defined as the ratio of the total optical power within a circle with a radius three times the full width at half maximum (FWHM) of the focal spot to the total power incident onto the metalens, maintains to be high across the visible region and exhibits an averaged value of 80.76% from 450 nm to 650 nm (orange curve, Fig. 2(c)). For calculating the device operational efficiencies in this study, we have filtered out the unmodulated co-polarization component and only accounted for the modulated cross-polarization component in the efficiency evaluation.

Spin-multiplexed metasurface dual-beam generator

We will further employ the developed method to design a spin-multiplexed metasurface dual-beam generator working at free-space wavelength of λ_0 = 532 nm. The device is capable of generating a zeroth-order Bessel beam under RCP illumination, and first-order Bessel beam under LCP illumination (Fig. 3(a)). The target EM response of such metasurface can be described by a Jones Matrix ($\mathbf{J}$) satisfying the following pair of equations:

$$e^{i\phi_1}\,|L\rangle = \mathbf{J}\,|R\rangle\ , \tag{4}$$

$$e^{i\phi_2}\,|R\rangle = \mathbf{J}\,|L\rangle\ , \tag{5}$$

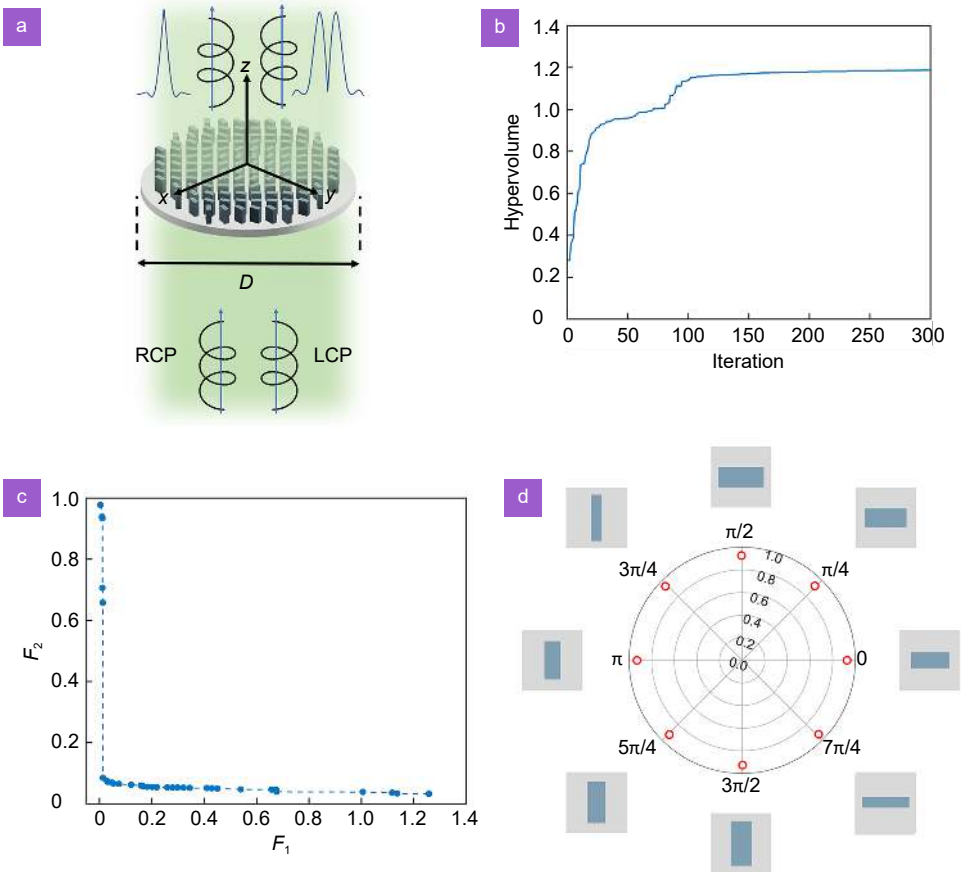

Fig. 3 | Spin-multiplexed metasurface dual beam generator. (**a**) Schematic depiction of the spin-multiplexed metasurface dual-beam generator with a diameter *D*, positioned in the *z* = 0 μm plane with its center at the coordinate origin. The device generates a zeroth-order Bessel beam under right-handed circular polarized (RCP) illumination and a first-order Bessel beam under left-handed circular polarized (LCP) illumination. (**b**) Hypervolume plotted against iteration number. The hypervolume curve tends to plateau after approximately 250 iterations, indicating convergence of the genetic algorithm (GA). (**c**) Non-dominated front plot of the population in the final iteration of the algorithm. (**d**) Schematic illustration of the 8 meta-atom structures obtained through the GA optimization. Their electromagnetic (EM) performance at λ_0 = 532 nm is represented by red dots in a polar coordinate system, where the azimuthal angle denotes the phase shift modulation value (in radians) and the distance from the origin signifies the polarization conversion efficiency (PCE).

where ϕ_1 and ϕ_2 denote the phase modulation profile for the RCP ($|R\rangle$) and LCP ($|L\rangle$) incident light, respectively. The above equations indicate that the metasurface needs to impart independent and arbitrary phase shift modulations on the RCP and LCP illumination light. One way to implement such a device is to identify a group of meta-atoms that can i) act as half-wave plates at the target operational wavelength (λ_0 = 532 nm) and simultaneously, ii) provide high and evenly-spaced phase shift modulations for a linearly polarized (*x*- or *y*-polarized) incident light of λ_0 = 532 nm. The associated detailed discussions can be found in Refs.[51–54].

In this task, we choose to establish a meta-atom library consisting of 8 different meta-atoms that provide equally-spaced phase shift modulation values spanning a full 2π range. This can be done by first identifying 4 basic half-wave-plate-like meta-atom structures providing phase shift modulation covering half of the 2π range, and then get the other 4 meta-atom structures by in-plane rotating the 4 basic structures by 90°. Similar to the first design task, we also choose to employ TiO_2-based nanofin-shaped structures to construct the metasurface. The variables of the GA algorithm include the period (*p*), height (*h*), as well as the lateral width (*w*) and length (*l*) of the nanofin-shaped meta-atom. Different from the earlier task, each individual now consists of 10 variables, namely, the period (*p*) and height (*h*) which the 4 meta-atoms share, and 4 sets of lateral width and length (w_1–w_4, l_1–l_4) of the meta-atoms. The ranges of variation for *p* and *h* are respectively set to be 250–450 nm and 100–800 nm. The range of variation for the cross-sectional dimensions (w_1–w_4, l_1–l_4) are all constrained within 50 ~ (*p* - 40) nm. Two fitness functions (F_1 and F_2) are respectively defined to evaluate the meta-atom's even-spaced phase shift modulation coverage and half-wave-plate-like response.

$$F_1 = \frac{1}{3}\sum_{i=1}^{3}\left|\Delta\phi_i - \frac{\pi}{4}\right| + \sqrt{\frac{1}{3}\sum_{i=1}^{3}\left(\Delta\phi_i - \overline{\Delta\phi}\right)^2}\,, \tag{6}$$

$$F_2 = 1 - PCE_{\min}\,. \tag{7}$$

Fitness function F_1 evaluates the even-spaced phase shift coverage of the meta-atoms, where $\Delta\phi_i$ (i = 1, 2, 3) represents the phase shift modulation intervals among the 4 structures in each individual. $\overline{\Delta\phi}$ is the average value of the 3 phase shift modulation intervals within an individual. Fitness function F_2 evaluates the half-wave-plate-like response of the meta-atoms, where PCE_{min} is the smallest PCE value of the four meta-atom structures in one individual. In order to rule out the interference of any resonance effect, the PCE value of each meta-atom is averaged at three adjacent wavelengths of 527 nm, 532 nm, and 537 nm. Figure 3(b) plots the value of hypervolume as a function of iteration number. The hypervolume curve tends to flatten after ~250 iterations, indicating the convergence of the GA algorithm. The non-dominated front plot of the population in the final iteration step is shown in Fig. 3(c). The 4 basic meta-atom structures selected through the optimization process have height of *h* = 600 nm and period of *p* = 350 nm. Table 1 lists key parameters of the meta-atoms, including their lateral dimensions (*w* and *l*), phase shift modulation values for *x*-polarized light (ϕ_x) and PCE values at λ_0 = 532 nm. The other 4 meta-atom structures can be obtained by in-plane rotating the above 4 structures by 90°. Figure 3(d) displays the PCE and phase shift modulation coverage of the 8 meta-atoms, where they all exhibit PCE higher than 90% and provide close-to-ideal even-spaced phase shift modulation for a *x*-polarized incident light of λ_0 = 532 nm.

Using the obtained meta-atom library, we implement a spin-multiplexed metasurface dual-beam generator occupying a circular area with a diameter of *D* = 50 μm. The output beam from the device can switch between two Bessel beams with different orders and NAs under RCP and LCP illuminations, respectively. The associated two distinct phase shift profiles are expressed as:

$$\phi_1(x,y) = -\frac{2\pi}{\lambda_0}NA_1\left(\sqrt{x^2+y^2}\right)\,, \tag{8}$$

Table 1 | Key parameters of the optimized meta-atoms for the spin-multiplexed metasurface dual-beam generator.

Lateral dimensions		Phase shift modulation value for *x*-polarized light	Polarization conversion efficiency
w (nm)	*l* (nm)	ϕ_x (rad)	PCE (%)
224	92	0.00	94.18
242	106	0.79	92.68
260	118	1.58	92.84
63	270	2.37	92.02

$$\phi_2(x,y) = -\frac{2\pi}{\lambda_0} NA_2 \left(\sqrt{x^2+y^2}\right) + \arctan\left(\frac{y}{x}\right) , \quad (9)$$

here, x and y are in-plane distances along orthogonal directions from the center of the circular shaped metasurface, given incident light propagating along the positive z-direction. We choose NA_1 = 0.7 and NA_2 = 0.3. To construct the metasurface, the meta-atom at a given coordinate location (x,y) should provide a phase shift modulation for x-polarized incident light that is closest to the required phase shift modulation value, $\phi_x(x,y)$,

$$\phi_x(x,y) = \frac{1}{2}\left(\phi_1(x,y) + \phi_2(x,y)\right) . \quad (10)$$

At the same time, the meta-atom's in-plane rotation angle, $\theta(x,y)$, should be set as:

$$\theta(x,y) = -\frac{1}{4}\left(\phi_1(x,y) - \phi_2(x,y)\right) . \quad (11)$$

The performance of the constructed spin-multiplexed metasurface dual-beam generator is evaluated thorough FDTD simulation. When illuminated by an RCP light at free-space wavelength of λ_0 = 532 nm, the transmitted beam is a zeroth-order Bessel beam with NA = 0.7 (Fig. 4(a)) and its horizontal cut (at z = 7 μm) fits well with the zeroth-order Bessel function (Fig. 4(b)). When the spin state of the illumination light is switched to LCP, the transmitted beam changes to a first-order Bessel beam with NA = 0.3 (Fig. 4(c)) and its horizontal cut (at z = 20 μm) exhibits a high degree of consistency with the first-order Bessel function (Fig. 4(d)). The FWHM widths of the zeroth-order and first-order Bessel beams are respectively 0.2733 μm and 0.5088 μm, all corresponding well with theoretical ones (0.2721 μm for the zeroth-order Bessel beam and 0.5178 μm for the first-order Bessel beam). To evaluate the generation efficiency of the dual-functional metasurface, we first identify a cross-section where the generated beam exhibits the highest intensity. The efficiency is then computed as the ratio of the total optical power within a circle with a radius three times the FWHM of the generated Bessel beam's intensity profile to the total incident power on the metasurface. The generation efficiency is calculated to be 88.07% and 90.72% for RCP and LCP illuminations, respectively.

Wavelength and spin co-multiplexed four-channel metahologram

Finally, we employ the developed method to design a

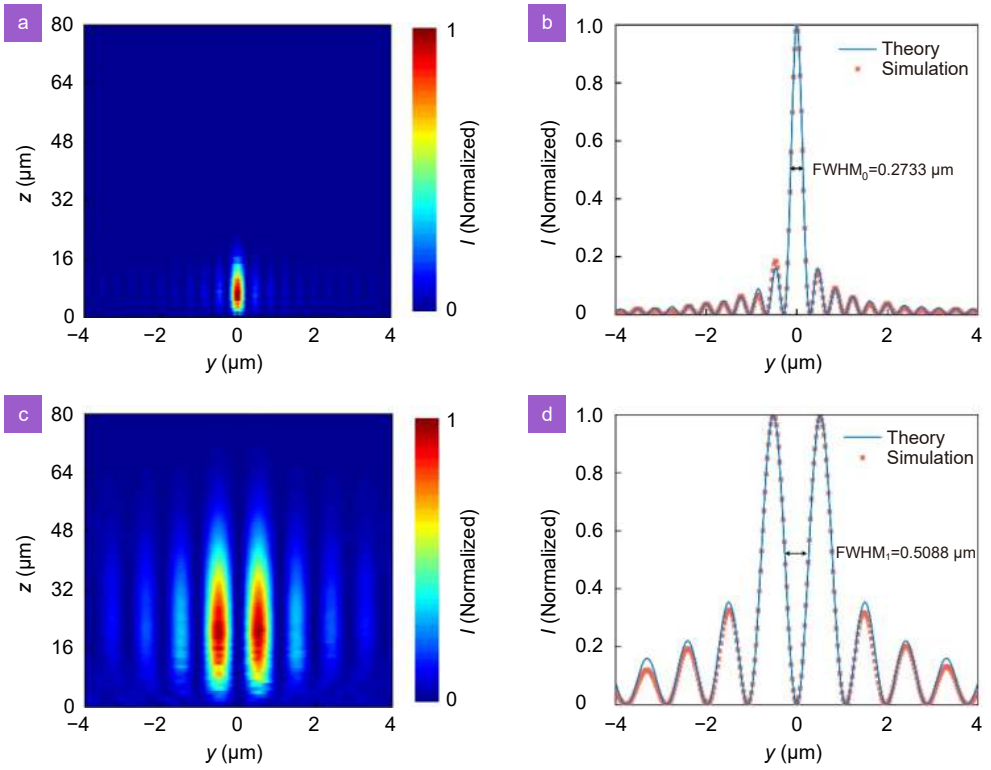

Fig. 4 | Bessel beams generated by the optimized spin-multiplexed metasurface. (**a**, **b**) The normalized intensity profile of the zeroth-order Bessel beam (NA_1 = 0.7) in the y-z plane at free-space RCP illumination of λ_0 = 532 nm (a) and its corresponding horizontal cut at z = 7 μm (b). (**c**, **d**) The normalized intensity profile of the first-order Bessel beam (NA_2 = 0.3) in the y-z plane at free-space LCP illumination of λ_0 = 532 nm (c) and its corresponding horizontal cut at z = 20 μm (d).

wavelength and spin co-multiplexed four-channel metahologram. The device projects holographic images of the capital letters "H" and "S" respectively under RCP and LCP illumination at a free-space wavelength of 532 nm, and simultaneously, images of the letter of "U" and "T" under RCP and LCP illumination of free-space wavelength of 633 nm (Fig. 5(a)). The target EM response of such metasurface can be described by a Jones Matrix ($\mathbf{J}$) satisfying the following equation:

$$e^{i\phi_{0,1}^{-,+}}|\lambda_{0,1}^{-,+}\rangle = \mathbf{J}|\lambda_{0,1}^{+,-}\rangle \ , \tag{12}$$

where ϕ_0^- and ϕ_0^+ denote the phase modulation profile for the LCP ($|\lambda_0^+\rangle$) and RCP ($|\lambda_0^-\rangle$) incident light at free-space wavelength of λ_0 = 532 nm, respectively. ϕ_1^- and ϕ_1^+ denote the phase modulation profile for the LCP ($|\lambda_1^+\rangle$) and RCP ($|\lambda_1^-\rangle$) incident light at free-space wavelength of λ_1 = 633 nm, respectively. This equation indicates that the metahologram imparts independent and arbitrary phase shift modulation over the LCP and RCP illumination light at the two specific wavelengths. One way to implement such a device is to identify a group of meta-atoms that can (i) provide close to half-wave-plate-like responses at the two target operational wavelengths (532 nm and 633 nm), (ii) offer high and close to evenly-spaced phase shift modulations for a linearly polarized (*x*- or *y*-polarized) incident light at both wavelengths.

In this task, we choose to establish a meta-atom library consisting of 16 different meta-atoms that satisfy the aforementioned requirements. Similar to the previous task, we use TiO_2-based nanofins to construct the metasurface. The variables of the GA algorithm include

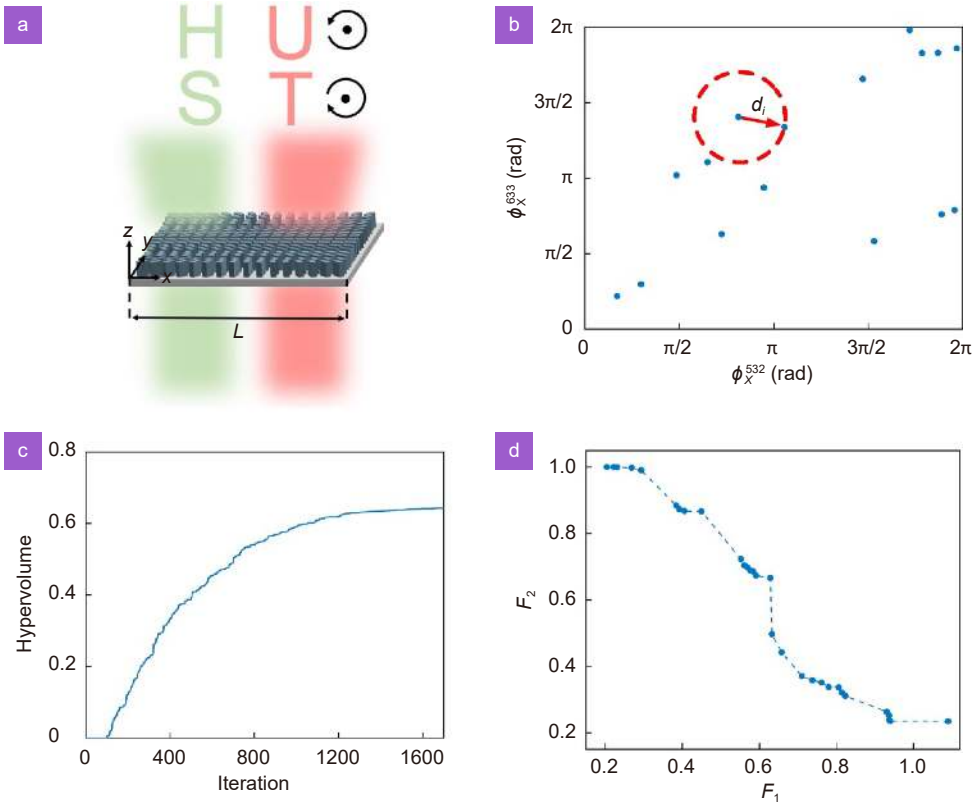

Fig. 5 | Wavelength and spin co-multiplexed four-channel metahologram. (**a**) Schematic depiction of the wavelength and spin co-multiplexed four-channel metahologram with a side length *L*, positioned in the *z* = 0 μm plane with its corner at the coordinate origin. The letters "H" and "S" are reconstructed at the *z* = 150 μm plane, under the RCP and LCP illumination at free-space wavelength of λ_0= 532 nm. The letters "U" and "T" are reconstructed at the same plane, under the RCP and LCP illumination at free-space wavelength of λ_1= 633 nm. (**b**) Phase shift modulation plot of the 16 meta-atom structures obtained through the final iteration of the GA optimization. The meta-atoms are represented as blue points, with their coordinates representing the phase shift modulation values for *x*-polarized incident light under wavelengths of 532 nm and 633 nm. d_i represents the distance from the *i*-th point to its nearest point in the coordinate system. For the clarity of display, we draw a red dashed circle centered at the *i*-th point with a radius of d_i, where the nearest point lies on the circle. (**c**) Hypervolume plotted against iteration number. The hypervolume curve tends to plateau after approximately 1700 iterations, indicating convergence of the GA. (**d**) Non-dominated front plot of the population in the final iteration of the algorithm.

the period (p), height (h), as well as the lateral length (l) and width (w) of the nanofin-shaped meta-atom. Each individual consists of 34 variables: the period (p) and height (h) which the 16 meta-atoms share, and 16 sets of lateral width and length (w_1–w_{16}, l_1–l_{16}) of the meta-atoms. The ranges of variation for p and h are respectively set to be 250–450 nm and 100–1000 nm. The range of variation for the cross-sectional dimensions (w_1–w_{16}, l_1–l_{16}) are all constrained within 50 ~ (p − 30) nm. The phase shift modulation values provided by each meta-atom for x-polarized incident light at the two target operational wavelengths are represented as a coordinate point in a 2D Cartesian coordinate system, with the axes denoting the phase shift modulation for wavelengths of 532 nm and 633 nm, respectively. Two fitness functions (F_1 and F_2) are respectively defined to evaluate the meta-atom's uniform phase shift modulation coverage and half-wave-plate-like response.

$$F_1 = \frac{1}{16}\sum_{i=1}^{16}\left|d_i - \frac{\pi}{2}\right| + \sqrt{\frac{1}{16}\sum_{i=1}^{16}(d_i - \bar{d})^2}\,, \tag{13}$$

$$F_2 = 1 - PCE_{\min}\,. \tag{14}$$

Fitness function F_1 evaluates the uniform phase shift coverage of the meta-atoms, where d_i (i = 1, 2, ..., 16) represents the distance from coordinate point of the i-th meta-atom to its nearest point in the 2D coordinate system. As an example, Fig. 5(b) plots the distribution of the 16 coordinate points for the optimized individual after the last iteration. $\bar{d}$ is the average value of the all 16 distances within an individual. Fitness function F_2 evaluates the half-wave-plate-like response of the meta-atoms, where PCE_{min} is the smallest PCE value at two target wavelengths of the 16 meta-atom structures in an individual. Figure 5(c) plots the value of hypervolume as a function of iteration number. The hypervolume curve tends to flatten after ~1700 iterations, indicating the convergence of the GA algorithm. The non-dominated front plot of the population in the final iteration step is shown in Fig. 5(d). The 16 basic meta-atom structures selected through the optimization process have height of h = 990 nm and period of p = 330 nm. Table 2 lists the key parameters of the obtained meta-atoms, including their lateral dimensions (w and l), phase shift modulation values for x-polarized light at two target wavelengths (ϕ_x^{532} and ϕ_x^{633}), and average polarization conversion efficiency for the two wavelengths (PCE_{mean}). The average PCEs of the meta-atoms at free-space wavelength of 532 nm and 633 nm are 59.91% and 78.15%, respectively.

Using the obtained meta-atom library, we implement a wavelength and spin co-multiplexed four-channel metahologram occupying a square area with a side length of L = 150 μm. Gerchberg-Saxton (GS) algorithm is employed to calculate the phase shift profiles, $\phi_0^+(x,y)$, $\phi_1^+(x,y)$, $\phi_0^-(x,y)$ and $\phi_1^-(x,y)$, required to project a holographic "H", "U", "S" and "T" image (150 μm in width) located in the z = 150 μm plane, respectively, under illumination at free-space wavelengths of 533 nm,

Table 2 | Key parameters of the optimized meta-atoms for the wavelength and spin co-multiplexed four-channel metahologram.

Lateral dimensions		Phase shift modulation values for x-polarized light		Average polarization conversion efficiency
w (nm)	l (nm)	ϕ_x^{532} (rad)	ϕ_x^{633} (rad)	PCE_{mean} (%)
186	57	6.15	2.48	57.43
300	54	2.55	4.41	74.42
118	247	2.04	3.47	77.08
271	144	2.28	1.97	94.16
164	300	0.93	0.93	79.26
212	90	3.32	4.20	71.76
160	300	0.53	0.69	85.06
134	300	4.62	5.20	82.76
144	292	5.61	5.74	88.98
262	187	2.98	2.94	37.37
97	218	5.93	2.39	65.95
75	249	4.81	1.83	66.42
164	214	5.87	5.75	40.29
219	62	1.52	3.20	75.04
261	100	5.40	6.22	59.90
271	91	6.18	5.84	48.54

633 nm, 532 nm, and 633 nm. Here, x and y are in-plane distances along orthogonal directions from the corner of the coordinate system where the square shaped metasurface located, given incident light propagating along the positive z-direction. To construct the metasurface, the meta-atom at a given coordinate location (x, y) should provide phase shift modulations for the two target wavelengths closest to the required phase shift modulation values, $\phi_x^{532}(x,y)$ and $\phi_x^{633}(x,y)$,

$$\phi_x^{532}(x,y) = \frac{1}{2}\left(\phi_0^+(x,y) + \phi_0^-(x,y)\right) , \tag{15}$$

$$\phi_x^{633}(x,y) = \frac{1}{2}(\phi_1^+(x,y) + \phi_1^-(x,y)) . \tag{16}$$

At the same time, the meta-atom's in-plane rotation angle, $\theta(x,y)$, should be set as:

$$\theta(x,y) = -\frac{1}{8}\left(\phi_0^+(x,y) - \phi_0^-(x,y) + \phi_1^+(x,y) - \phi_1^-(x,y)\right) . \tag{17}$$

We evaluate the performance of the constructed metahologram thorough FDTD simulation. Figure 6 displays the simulated holographic imaging results. As expected, four images are selectively projected onto the target plane, depending on the combination of free-space wavelength (532 nm or 633 nm) and spin state (RCP or LCP) of the illumination light. The device operational efficiency, defined as the ratio of the optical power of the projected holographic image to the power illuminating the metahologram, is calculated to be 53.24% (RCP illumination) and 52.45% (LCP illumination) at 532 nm, and 62.06% (RCP illumination) and 60.90% (LCP illumination) at 633 nm.

Conclusions

In summary, we introduce a genetic algorithm assisted meta-atom design approach that is efficient and effective for both single- and multi-objective metasurface design tasks. The developed method incorporates a comprehensive set of parameters describing the meta-atoms, including constituent material, period, height, and lateral sizes, as variables of an individual during the optimization process. Similar to natural selection and evolution processes, a population of individuals undergoes multiple iterations of selection, crossover, and mutation, continually adjusting their chromosomes (i.e., meta-atom variables) to minimize the fitness function values which reflect the design targets. This iterative process culminates in globally optimized parameter sets that best fulfill the desired device functionalities. Through the application of our

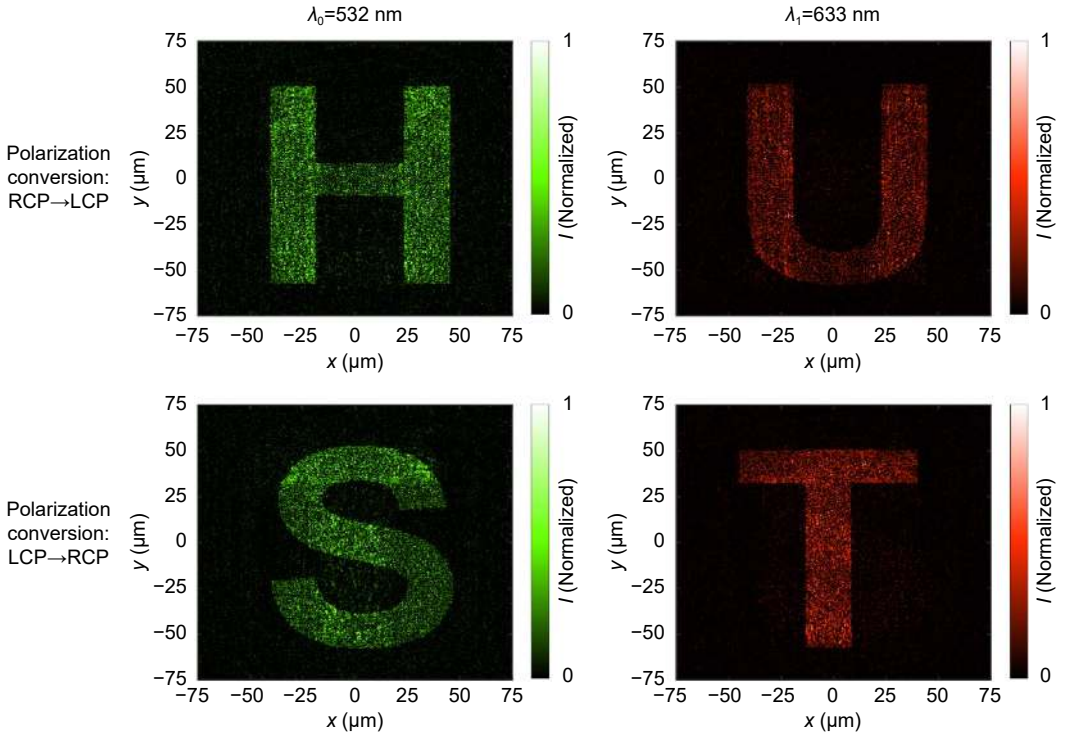

Fig. 6 | Simulated holographic imaging results of the four-channel metahologram. Four images (capital letters "H", "U", "S" and "T") are selectively projected into the target plane, depending on the combination of free-space wavelength (532 nm or 633 nm) and spin state (RCP or LCP) of the illumination light. The image plane is located 150 μm above the metahologram device.

developed method, we showcase the design of three high-performance metasurface devices operating in the visible spectrum. Specifically, we present a broadband Pancharatnam-Berry phase-based metalens with an average focusing efficiency exceeding 80% from 450 nm to 650 nm, a spin-multiplexed structural beam generator which generates two different Bessel beams depending on the spin of the illumination light and exhibits operational efficiencies surpassing 88% at 532 nm, and a wavelength and spin co-multiplexed four-channel metahologram which exhibits efficiencies exceeding 50% and 60% at 532 nm and 633 nm, respectively. In this work, the cross-sectional dimension of the meta-atom is constrained to be at least 30 nm smaller than the period, thereby minimizing the coupling effect between neighboring meta-atoms. In design tasks where the coupling of meta-atoms plays a significant role in their EM responses, the cross-sectional dimension of the meta-atom can be set to have a wider range of variation, and the EM simulation step in the algorithm can be adjusted to account for the coupling effect. Additionally, integrating optimization algorithms and machine learning methods for metasurface inverse design could offer additional advantages, which include accelerating computational speed[55,56], improving device functionality[57,58], and better accounting for near-field coupling effects[59]. Our work offers an effective and easily implementable approach for diverse meta-atom design and optimization tasks, thereby empowering designers to create high-performance metasurface optics across a range of operational bands and with a variety of functionalities.

Methods

The algorithm runs under python version 3.10, pymoo version 0.6.0, and grcwa version 0.1.2 on a workstation (Intel(R) Xeon(R) Gold 5218R CPU @ 2.10Hz with 512 GB RAM, running the Windows 10 operating system (Microsoft)). The runtimes for the three tasks are about 1 hour, 2 hours, and 31 hours, respectively.

References

1. Kuznetsov AI, Brongersma ML, Yao J et al. Roadmap for optical metasurfaces. *ACS Photonics* **11**, 816–865 (2024).
2. Liu ZY, Wang DY, Gao H et al. Metasurface-enabled augmented reality display: a review. *Adv Photonics* **5**, 034001 (2023).
3. Li LL, Zhao HT, Liu C et al. Intelligent metasurfaces: control, communication and computing. *eLight* **2**, 7 (2022).
4. Ding F, Pors A, Bozhevolnyi SI. Gradient metasurfaces: a review of fundamentals and applications. *Rep Prog Phys* **81**, 026401 (2018).
5. Li Y, Huang XJ, Liu SX et al. Metasurfaces for near-eye display applications. *Opto-Electron Sci* **2**, 230025 (2023).
6. Liu ZY, Gao H, Ma TG et al. Broadband spin and angle co-multiplexed waveguide-based metasurface for six-channel crosstalk-free holographic projection. *eLight* **4**, 7 (2024).
7. Luo XG. Principles of electromagnetic waves in metasurfaces. *Sci China Phys Mech Astron* **58**, 594201 (2015).
8. Guo YH, Zhang SC, Pu MB et al. Spin-decoupled metasurface for simultaneous detection of spin and orbital angular momenta via momentum transformation. *Light Sci Appl* **10**, 63 (2021).
9. Wang SM, Wu PC, Su VC et al. Broadband achromatic optical metasurface devices. *Nat Commun* **8**, 187 (2017).
10. Liu XY, Zhang JC, Leng BR et al. Edge enhanced depth perception with binocular meta-lens. *Opto-Electron Sci* **3**, 230033 (2024).
11. Zheng GX, Mühlenbernd H, Kenney M et al. Metasurface holograms reaching 80% efficiency. *Nat Nanotechnol* **10**, 308–312 (2015).
12. So S, Kim J, Badloe T et al. Multicolor and 3D holography generated by inverse‐designed single‐cell metasurfaces. *Adv Mater* **35**, 2208520 (2023).
13. Li X, Chen QM, Zhang X et al. Time-sequential color code division multiplexing holographic display with metasurface. *Opto-Electron Adv* **6**, 220060 (2023).
14. Chen WT, Khorasaninejad M, Zhu AY et al. Generation of wavelength-independent subwavelength Bessel beams using metasurfaces. *Light Sci Appl* **6**, e16259 (2017).
15. Zhang S, Huo PC, Wang YL et al. Generation of achromatic auto-focusing airy beam for visible light by an all-dielectric metasurface. *J Appl Phys* **131**, 043104 (2022).
16. Zhang JC, Chen MK, Fan YB et al. Miniature tunable Airy beam optical meta-device. *Opto-Electron Adv* **7**, 230171 (2024).
17. So S, Mun J, Park J et al. Revisiting the design strategies for metasurfaces: fundamental physics, optimization, and beyond. *Adv Mater* **35**, 2206399 (2023).
18. Ma W, Liu ZC, Kudyshev ZA et al. Deep learning for the design of photonic structures. *Nat Photonics* **15**, 77–90 (2021).
19. Elsawy MMR, Lanteri S, Duvigneau R et al. Numerical optimization methods for metasurfaces. *Laser Photonics Rev* **14**, 1900445 (2020).
20. Wiecha PR, Muskens OL. Deep learning meets nanophotonics: a generalized accurate predictor for near fields and far fields of arbitrary 3D nanostructures. *Nano Lett* **20**, 329–338 (2020).
21. Chen MK, Liu XY, Sun YN et al. Artificial intelligence in meta-optics. *Chem Rev* **122**, 15356–15413 (2022).
22. Jiang JQ, Sell D, Hoyer S et al. Free-form diffractive metagrating design based on generative adversarial networks. *ACS Nano* **13**, 8872–8878 (2019).
23. Liu ZC, Zhu DY, Raju L et al. Tackling photonic inverse design with machine learning. *Adv Sci* **8**, 2002923 (2021).
24. Wang DY, Liu ZY, Wang HZ et al. Structural color generation: from layered thin films to optical metasurfaces. *Nanophotonics* **12**, 1019–1081 (2023).
25. Shi ZJ, Zhu AY, Li ZY et al. Continuous angle-tunable birefringence with freeform metasurfaces for arbitrary polarization conversion. *Sci Adv* **6**, eaba3367 (2020).
26. Sell D, Yang JJ, Doshay S et al. Large-angle, multifunctional metagratings based on freeform multimode geometries. *Nano Lett* **17**, 3752–3757 (2017).
27. Yang JJ, Fan JA. Topology-optimized metasurfaces: impact of initial geometric layout. *Opt Lett* **42**, 3161–3164 (2017).

28. Whiting EB, Campbell SD, Kang L et al. Meta-atom library generation via an efficient multi-objective shape optimization method. *Opt Express* **28**, 24229–24242 (2020).
29. Zou XJ, Zhang YM, Lin RY et al. Pixel-level Bayer-type colour router based on metasurfaces. *Nat Commun* **13**, 3288 (2022).
30. Zhu DZ, Whiting EB, Campbell SD et al. Optimal high efficiency 3D plasmonic metasurface elements revealed by lazy ants. *ACS Photonics* **6**, 2741–2748 (2019).
31. Song CT, Pan LZ, Jiao YH et al. A high-performance transmitarray antenna with thin metasurface for 5G communication based on PSO (particle swarm optimization). *Sensors* **20**, 4460 (2020).
32. Holland JH. Genetic algorithms. *Sci Am* **267**, 66–73 (1992).
33. Fan YL, Xu YK, Qiu M et al. Phase-controlled metasurface design via optimized genetic algorithm. *Nanophotonics* **9**, 3931–3939 (2020).
34. Egorov V, Eitan M, Scheuer J. Genetically optimized all-dielectric metasurfaces. *Opt Express* **25**, 2583–2593 (2017).
35. Jafar-Zanjani S, Inampudi S, Mosallaei H. Adaptive genetic algorithm for optical metasurfaces design. *Sci Rep* **8**, 11040 (2018).
36. Li ZG, Stan L, Czaplewski DA et al. Broadband infrared binary-pattern metasurface absorbers with micro-genetic algorithm optimization. *Opt Lett* **44**, 114–117 (2019).
37. Deb K, Pratap A, Agarwal S et al. A fast and elitist multiobjective genetic algorithm: NSGA-II. *IEEE Trans Evol Comput* **6**, 182–197 (2002).
38. Blickle T, Thiele L. A mathematical analysis of tournament selection. In *Proceedings of the 6th International Conference on Genetic Algorithms* 9–15 (Morgan Kaufmann Publishers Inc. , 1995).
39. Deb K, Sindhya K, Okabe T. Self-adaptive simulated binary crossover for real-parameter optimization. In *Proceedings of the 9th Annual Conference on Genetic and Evolutionary Computation* 1187–1194 (ACM, 2007); http://doi.org/10.1145/1276958.1277190.
40. Deb K, Deb D. Analysing mutation schemes for real-parameter genetic algorithms. *Int J Artif Intell Soft Comput* **4**, 1–28 (2014).
41. While L. A new analysis of the LebMeasure algorithm for calculating hypervolume. In *Proceedings of the Evolutionary Multi-Criterion Optimization: Third International Conference* 326–340 (Springer, 2005); http://doi.org/10.1007/978-3-540-31880-4_23.
42. Xie X, Pu MB, Jin JJ et al. Generalized Pancharatnam-Berry phase in rotationally symmetric meta-atoms. *Phys Rev Lett* **126**, 183902 (2021).
43. Khorasaninejad M, Chen WT, Devlin RC et al. Metalenses at visible wavelengths: diffraction-limited focusing and subwavelength resolution imaging. *Science* **352**, 1190–1194 (2016).
44. Zhang C, Divitt S, Fan Q et al. Low-loss metasurface optics down to the deep ultraviolet region. *Light Sci Appl* **9**, 55 (2020).
45. Zhang C, Chen L, Lin ZL et al. Tantalum pentoxide: a new material platform for high-performance dielectric metasurface optics in the ultraviolet and visible region. *Light Sci Appl* **13**, 23 (2024).
46. Zhao D, Lin ZL, Zhu WQ et al. Recent advances in ultraviolet nanophotonics: from plasmonics and metamaterials to metasurfaces. *Nanophotonics* **10**, 2283–2308 (2021).
47. Colburn S, Zhan AL, Bayati E et al. Broadband transparent and CMOS-compatible flat optics with silicon nitride metasurfaces [Invited]. *Opt Mater Express* **8**, 2330–2344 (2018).
48. Tseng ML, Semmlinger M, Zhang M et al. Vacuum ultraviolet nonlinear metalens. *Sci Adv* **8**, eabn5644 (2022).
49. Devlin RC, Khorasaninejad M, Chen WT et al. Broadband high-efficiency dielectric metasurfaces for the visible spectrum. *Proc Natl Acad Sci USA* **113**, 10473–10478 (2016).
50. Liu MZ, Zhu WQ, Huo PC et al. Multifunctional metasurfaces enabled by simultaneous and independent control of phase and amplitude for orthogonal polarization states. *Light Sci Appl* **10**, 107 (2021).
51. Balthasar Mueller JP, Rubin NA, Devlin RC et al. Metasurface polarization optics: independent phase control of arbitrary orthogonal states of polarization. *Phys Rev Lett* **118**, 113901 (2017).
52. Fan QB, Zhu WQ, Liang YZ et al. Broadband generation of photonic spin-controlled arbitrary accelerating light beams in the visible. *Nano Lett* **19**, 1158–1165 (2019).
53. Huo PC, Zhang C, Zhu WQ et al. Photonic spin-multiplexing metasurface for switchable spiral phase contrast imaging. *Nano Lett* **20**, 2791–2798 (2020).
54. Zhang F, Guo YH, Pu MB et al. Meta-optics empowered vector visual cryptography for high security and rapid decryption. *Nat Commun* **14**, 1946 (2023).
55. Shameli MA, Fallah A, Yousefi L. Developing an optimized metasurface for light trapping in thin-film solar cells using a deep neural network and a genetic algorithm. *J Opt Soc Am B* **38**, 2728–2735 (2021).
56. Zhang JM, Wang GW, Wang T et al. Genetic algorithms to automate the design of metasurfaces for absorption bandwidth broadening. *ACS Appl Mater Interfaces* **13**, 7792–7800 (2021).
57. Ma W, Xu YH, Xiong B et al. Pushing the limits of functionality - multiplexing capability in metasurface design based on statistical machine learning. *Adv Mater* **34**, 2110022 (2022).
58. Zhu DY, Liu ZC, Raju L et al. Building multifunctional metasystems *via* algorithmic construction. *ACS Nano* **15**, 2318–2326 (2021).
59. An SS, Zheng BW, Shalaginov MY et al. Deep convolutional neural networks to predict mutual coupling effects in metasurfaces. *Adv Opt Mater* **10**, 2102113 (2022).

Acknowledgements

ZJ Yu, MX Li, ZY Xing, H Gao, ZY Liu, and C Zhang acknowledge the support from the National Science Foundation of China (Grant Nos. 62075078 and 62135004) and the Knowledge Innovation Program of Wuhan-Shuguang Project (Grant No. 2022010801020095).

Competing interests

The authors declare no competing financial interests.

Scan for Article PDF